

Contribution of Emulsion Zone in Refining of Basic Oxygen Steelmaking Converter



PRASENJIT SINGHA

The importance of emulsion zone formation in the basic oxygen steelmaking (BOF) process lies in its crucial role in enhancing refining efficiency. This study provides a comprehensive theoretical analysis of refining in BOF steelmaking, empowering steelmakers to optimize emulsion zone formation. By examining the contributions of decarburization, desiliconization, and dephosphorization from the emulsion zone, the study systematically investigates refining phenomena in distinct sections of the BOF converter, interconnected through recirculation streams. By utilizing FactSage™ and its macro-facilities, transient variations in metal and slag compositions, alongside varying terminal phosphorus levels for diverse emulsion zone dimensions, are quantified. Model findings highlight that emulsion and hotspot zones play roles in decarburization and desiliconization, while dephosphorization exclusively occurs within the emulsion zone. The model's projections for carbon, silicon, and phosphorus removals (wt pct) and metal bath temperature concur with data obtained from plant trials. This comprehensive analysis enhances our understanding of the BOF steelmaking process, enabling steelmakers to fabricate the required emulsion zone strategically for optimal refining efficiency.

<https://doi.org/10.1007/s11663-024-03117-y>

© The Minerals, Metals & Materials Society and ASM International 2024

I. INTRODUCTION

UNDERSTANDING the thermodynamic principles that influence the dephosphorization of steel is critical because dephosphorization is a complex multiphase reaction. To effectively remove phosphorus, it is essential to ensure sufficient emulsion formation. Ogasawara *et al.*^[1] demonstrated an experimental increase in dephosphorization rate by reusing slag post-decarburization, achieved by elevating the oxygen flow rate and iron ores. Pahlevani *et al.*^[2] showcased that the distribution ratio of phosphorus, activity coefficient of P₂O₅, and slag nature are contingent on the CaO content in the liquid slag. Wu *et al.*^[3] documented the uniform growth of phosphorus, mainly combined with CaO-SiO₂ and C₂S crystal, into spherical shapes when the slag basicity closely approaches 3. Bauri *et al.*^[4] developed a model utilizing multiple linear regression to predict the phosphorus partition ratio, comparing the results with plant data. The Nippon Steel Corporation^[5–9] has contributed insights into energy conservation by integrating dephosphorization and decarburization in a single converter. Notably, Wagner, Yang *et al.*^[10,11] emphasized the dependence of the dephosphorization index on the

equilibrium between gas-slag and slag-metal interactions. He and Zhang^[12] predicted the endpoint phosphorus content based on principal component analysis (PCA) and BP neural networks. They used an MLR model and a pure BP neural network model to calculate the endpoint phosphorus content. Sun *et al.*^[13] introduced dephosphorization characteristics using the ion-molecule coexistence theory (IMCT), and they found that by increasing the phosphorus enrichment contribution ratio of 2CaO-SiO₂ in slag, the dephosphorization capacity of slag was enhanced. Turkdogan and Pearson^[14,15] illustrated an estimation of the phosphorus partition ratio for reaction $2[P] + 5(O) = (P_2O_5)$. Chen and He^[16] demonstrated that MgO content in slag has an essential effect on the phosphorus distribution ratios. They showed that the average phosphorus distribution ratio reduces remarkably from 120.7 to 75.7 when the average MgO content in the end-blowing slag increases from 7.0 to 9.8 pct, owing to thermodynamics and kinetics reasons. Dephosphorization and refractory wear are minimized by fixing the MgO content between 6 and 8 pct. Keda and Matsuo^[17] experimentally demonstrated that basicity has an essential effect on dephosphorization. They found from experimental results that the higher the total iron oxide content in the slag, the more dephosphorization occurs. To obtain a higher degree of dephosphorization, the slag's iron content should be high when the SiO₂ content in the slag is high. Studies^[18,19] have reported an increase in

PRASENJIT SINGHA is with the Department of Metallurgical and Materials Engineering, Indian Institute of Technology Madras, Chennai, Tamil Nadu, India. Contact e-mail: psinghnift@gmail.com
Manuscript submitted February 28, 2024; accepted April 24, 2024.
Article published online May 16, 2024.

endpoint phosphorus due to rising temperatures from 1590 °C to 1660 °C, even within a basicity range of 1.75 to 3.14. Deo and Boom^[20] introduced dephosphorization and reversion of phosphorus behavior in the emulsion zone of the basic oxygen steelmaking process and basicity as well as early blowing of silicon and manganese oxidation effects on dephosphorization. Coley *et al.*^[21–24] presented decarburization and dephosphorization kinetics by considering droplet growth, nucleation, and CO gas bubbles with droplets using X-ray fluoroscopy. They introduced metal, slag chemistries, and behaviors of droplet formation rate. The existing process models of converter steelmaking can predict the end-blow parameters of the BOF process, including temperature, duration of the oxygen blowing, and the chemical compositions of slag and steel, with tolerable accuracy. Studies^[19,25,26] have investigated dephosphorization behaviors based on double slag operations for producing low-phosphorus steels. They proposed that the dephosphorization rate increased with increasing basicity up to 6. Further increase in the basicity of the second slag operation had minimal effect on dephosphorization. Basu *et al.*^[27–29] showed the effect of basicity (pct CaO/pct SiO₂) on the solubility of MgO in CaO-SiO₂-FeO-MgO-P₂O₅ at 1873 K, slag containing pct15 FeO and pct P₂O₅ is 4.5 as well as FeO, MgO contents and basicity (> 2.5) has an essential effect on dephosphorization index.

The presented works, ranging from,^[1–29] comprehensively illustrate instances of dephosphorization phenomena. These instances have been examined through computational simulations and experimental investigations, albeit within restricted process conditions.

Kozakevitch *et al.*^[30] and Meyer *et al.*^[31] illustrated that emulsion zones are mainly responsible for the decarburization reaction. Okano *et al.*^[32] and Price^[33] reported that the hotspot zone only involves decarburization reactions. In contrast, Chatterjee *et al.*^[34] claimed that metal droplets are responsible only for 35 pct to 40 pct of total decarburization. Other studies^[35–38] demonstrated that the contribution of decarburization

comes more or less from hotspots and emulsion zones. Singha and Shukla^[39] demonstrated decarburization behavior for different hotspot zone sizes.

Nevertheless, despite numerous conducted studies, the challenge persists in understanding the significance of the emulsion zone—a task complicated by the influence of multiple reactors, the minimization of free energy, and the diverse kinetic reactions taking place in both the impact and emulsion zones.

This investigation focuses on examining multiple smaller-size zones within the BOF converter, meticulously considering their interactions with each other. These zones collectively describe distinct portions of the converter. The overarching objective of this study is to provide predictive insights into the emulsion zone concerning decarburization, desiliconization, and dephosphorization. The study analyzed the behavior of decarburization, desiliconization, and dephosphorization for different sizes of the emulsion zone, along with considerations of slag composition and temperature.

II. MODEL AND PROCESS DESCRIPTION

The BOF converter's structural configuration (Figures 1(a) and (b)) can be conceptualized as having distinct regions, *i.e.*, the reactions in several zones (hotspot, emulsion, metal bath, slag bath, metal homogenization, and slag homogenization zones) were treated separately. This study used a reactor-based approach to transform mass transfer kinetic-based models for BOF steelmaking where reacting phase interfaces are in thermodynamic equilibrium. The core concept of reactor calculation is based upon multicomponent mixed transport theory, as given by^[40] a long time ago. The lower segment mirrors a metal bulk bath, wherein the dissolution of scrap occurs. Conversely, the upper portion corresponds to a slag bath, where simultaneous heat and mass transfer drive the dissolution of lime, dolomite, and iron ore. Within this investigation, the hotspot zone pertains to the interface where a

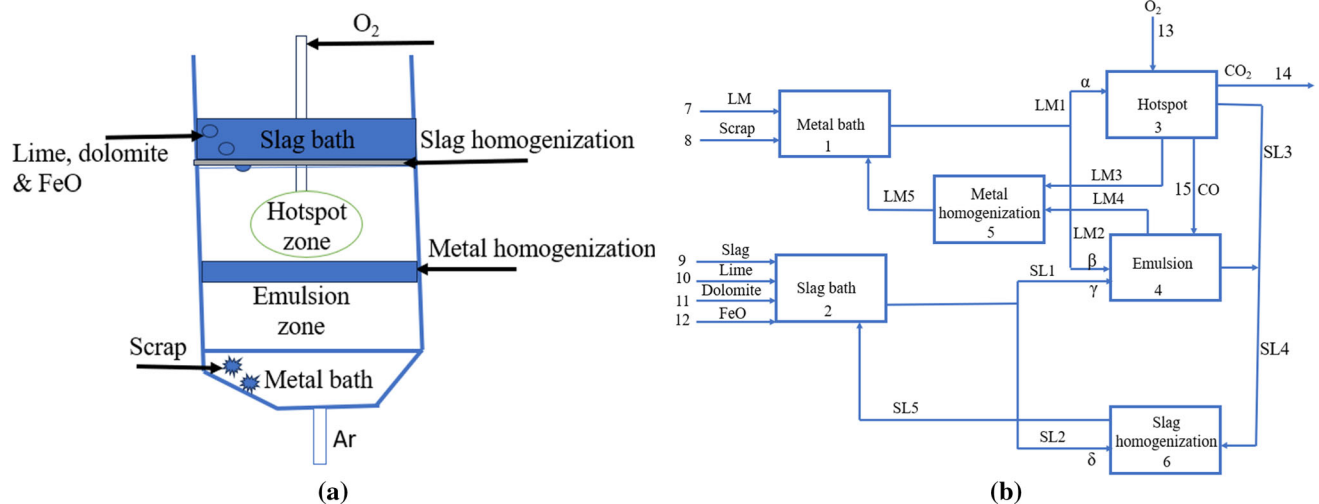


Fig. 1—(a) Single BOF converter (b) several zones connected through streams.

high-velocity oxygen jet impinges upon the metal bath from the lance. This locale serves as the site for oxidation processes involving carbon, silicon, manganese, and phosphorus in the hotspot zone. In the residual sector of the converter, known as the emulsion zone, within this zone, further oxidation of carbon, silicon, manganese, and phosphorus takes place alongside the occurrence of the emulsion phenomenon. Slag homogenization occurs between the hotspot and slag bath zone because the stirring intensity is high due to the oxygen supply at supersonic velocity. Similarly, metal homogenization occurs between the hotspot and emulsion zone. Two homogenization baths were added for homogenized temperature and the compositional difference between hotspot and emulsion and hotspot and slag bath. Notably, equilibrium is reached for each reaction within its corresponding reactor at discrete intervals. As reactions progress, the metal and slag phases migrate from the reaction zone back to their respective bulk phases from the metal and slag homogenization baths, respectively, thereby perpetuating the refining process. Calculations involving inputs from the FToxid, FTmisc, and FactPS databases of FactSageTM^[41] were incorporated to analyze various reactors. FactSageTM is a powerful thermodynamic software package widely used in materials science and metallurgy research. The prediction capabilities depend on the robustness of the databases employed for the calculations.

[FToxid]: This database system is fully optimized for the FeO-SiO₂-Al₂O₃-CaO-MgO-MnO-P₂O₅ system.

[FTmisc]: It is fully optimized for the Fe-C-Si-Mn-P system.

These two systems' sub-binaries, sub-ternary and sub-quaternary, have also been optimized. This means that thermodynamic calculations for the above two systems can be performed in any composition range as a function of temperature.

[FactPS]: Gas phase containing mainly CO and CO₂ FactSage Macro Processing, an advanced capability, is utilized for the concurrent construction of kinetic calculation. FactSage databases play a pivotal role in facilitating equilibrium calculations for this purpose.

The work integrates FToxide, FTmisc, and FactPS databases^[42] and macro programs to perform calculations depending on the process conditions.

This metal processing system introduces a mixture of liquid metal and scraps into a metal bath through streams 7 and 8. Concurrently, slag (stream 9), lime (stream 10), dolomite (stream 11), and iron oxide (stream 12) are introduced into the slag bath. An oxygen jet (stream 13) is directed into the hotspot zone, where it dissolves in the liquid steel, promoting the oxidation of elements such as carbon (C), silicon (Si), manganese (Mn), and phosphorus (P). A circulation stream is extracted from the metal bath (LM1) and reintroduced at various stages within the hotspot zone to ensure a continuous process. The resulting liquid metal (LM3) and liquid slag (stream SL3) continuously go to the metal and slag homogenization baths. Carbon dioxide (CO₂) gas, generated within the hotspot zone, is released into the atmosphere. In the emulsion zone, streams LM2 and SL1, originating from the metal and

slag bulk baths, are systematically introduced at each step. Carbon monoxide (CO) gas, produced in the hotspot zone, is utilized as a reducing agent upon entering the emulsion zone. The liquid metal (LM4) and liquid slag (SL4) produced likewise go to the metal and slag bulk homogenization baths. Metal and slag return from metal and slag bulk homogenization baths to their bulk baths (reactors 1 and 2) at each time step, respectively.

A. Metal Flow Rate Calculation

The current study focuses on understanding the dynamics of metal fractions within the system, particularly α (LM1) and β (LM2), which represent the fractions of metal migrating toward the hotspot and emulsion zones. Additionally, γ (SL1) signifies the proportion of slag that enters the emulsion zone. These fractions are pivotal as they govern the refining processes under investigation. A fraction of liquid metal and slag is considered to be the function of mass transfer coefficients. The mass transfer coefficients in a basic oxygen steelmaking converter are affected by the energy rate introduced into the system through the top oxygen supply and bottom stirring system. The mixing energy is imparted to the system by two components. First, it is due to rising bottom stirring gases, and second, it is due to the impact of top-blown oxygen lance. The fraction of reacting phases at each time step depends on the circulation flow rates in liquid melt depending on the top-blowing energy and bottom-stirring system, and the slag flow rate depends on the mass transfer coefficients of metal and slag.

The impact of the top lance and bottom gas stirring system is computed using mathematical formulations (Eqs. [1] and [2]) earlier proposed by.^[39,43]

$$E_{Top}^0 = 6.32 \times 10^{-7} C_{os} \theta \frac{MQ^3}{WXn^2d^3} \quad [1]$$

$$E_b^0 = \frac{6.18Q_b T_{avg}}{W_m} \left(\ln \left(1 + \frac{g\rho_m H_m}{P_a} \right) + 0.06 \left(1 - \frac{T_0}{T_{avg}} \right) \right) \quad [2]$$

$$\alpha = 0.09 \left(\frac{E_{Top}^0}{8000} \right)^{0.5} \quad [3]$$

$$\beta = k \left(\frac{E_b^0}{8000} \right)^{0.5} \quad [4]$$

$$\frac{\gamma}{\beta} = 7 \text{ and } \gamma = \delta \quad [5]$$

The equation involves the calculation of the square root of the quotient of the total input energy and a fixed constant value of 8000.

To explore the impact of emulsion zone size (β), alterations in the k values were implemented, encompassing a range from 0.01 to 0.08. It's important to emphasize that the values of other fractions, such as α and γ , were held as constants throughout the simulation experiments. For a more detailed grasp of the calculations regarding metal spitting, refer to prior studies.^[39,44] Under identical conditions of composition and temperature, the flow rates of liquid metal, represented as α and β , exhibit variations. The study's overarching goal is to elucidate the influence of various parameters on the refining phenomena for different emulsion zones. It is known that some fixed amounts of metal react only with a fixed amount of slag. This fixed ratio was calculated based on their mass transfer coefficient. In this work, γ over $\beta = 7$ is found to be the best fit for plant data.

B. Methods and Materials

A turn-down converter collected a sample of metal during the blowing process. Sampling occurred at intervals of 4, 8, 12, 16, and 20 minutes from the start of blowing. Each heat yielded a single metal sample with thermocouple temperature measurements taken immediately before sampling. For each sampling instance, a minimum of six samples were obtained. After water-cooling, the samples underwent cutting, grinding, and polishing. The chemical composition of the samples was determined by employing a standard spectrometer.

The decarburization is calculated as follows:

$$\frac{dC}{dt} = (\text{wt pct carbon at initial in metal bath} \times \text{total wt of initial liquid metal} - \text{wt pct carbon in the metal bath at } i^{\text{th}} \text{ step} \times \text{total weight of the liquid metal in the metal bath at } i^{\text{th}} \text{ step}).$$

$$\left(\frac{dC}{dt}\right)_{\text{hotspotzone}} = (\text{wt pct carbon at initial in hotspot zone} \times \text{total wt. of initial liquid metal in hotspot zone} \times \alpha - \text{wt pct carbon at } i^{\text{th}} \text{ step in hotspot zone} \times \text{total weight of liquid metal at } i^{\text{th}} \text{ step in hotspot zone}).$$

$$\left(\frac{dC}{dt}\right)_{\text{emulsionzone}} = (\text{wt pct carbon at initial in emulsion zone} \times \text{total weight of the initial liquid metal in emulsion zone} \times \beta - \text{wt pct carbon at } i^{\text{th}} \text{ step in emulsion zone} \times \text{total weight of the liquid metal at } i^{\text{th}} \text{ step in emulsion zone}).$$

Desiliconization and dephosphorization were calculated with a similar approach to decarburization.

Where i denote the time step and $i = 1$ to 20.

C. Model Assumptions

1. At the interface, metal-gas, slag-metal, and slag-gas reactions occur exclusively, with refining rates governed by mass transfer in both the metal and slag phases.
2. The dissolution of lime and dolomite happened linearly over time, with consistent initial particle diam-

eters for both minerals are across all additions at different time steps.

3. In the initial 2 minutes of blowing, the iron ore was introduced, with the assumption that complete dissolution of the iron ore took place during this period.
4. The total blowing time is 20 minute, and the time step is 1 minute.

III. RESULTS

In the present work, a dynamic control model was developed based on the initial input parameters of Table I and the charging sequence of Table II using FactSageTM and its macro program facility.

A. Transient Carbon Behaviors

Figure 2 presents the graphical representation of variations in different parameters: wt pct carbon ('a'), total decarburization rate ('b'), decarburization from the hotspot zone ('c'), and decarburization from the emulsion zone ('d'). These variations are observed across various emulsion zone sizes as a function of the blowing time. From the insights in Figure 2(b), distinct decarburization rates are observed for k values ranging from 0.01 to 0.08. During the initial 5 minutes (1–5 min), the rates are 0.178, 0.182, 0.191, 0.201, and 0.221 tons per

Table I. Input Feature to Check the Present Model Performance

Input Materials	Element	Wt Pct
hot metal 144 tons	carbon	4.5
	manganese	0.35
	silicon	0.51
	sulfur	0.0024
scrap 11 tons	phosphorous	0.06
	carbon	0.22
	manganese	0.20
	silicon	0.020
dolomite 3.1 tons	sulfur	0.0023
	MgO	60
	CaO	40
lime 10.1 tons	CaO	96
initial hot metal temperature	SiO ₂	4
blowing time (min)	1312 °C	
O ₂ flow rate (Nm ³ /min)	20	
iron ore	455	
retained slag	mass in tons	2.1
	3 tons	11 pct SiO ₂ , 42 pct CaO, 12 pct MgO, 27 pct FeO and 4 pct MgO
Plant data.		

Table II. Charging Trajectory (LM, Scrap, Flux, and Oxygen)

Sl. No	Charge Quantity	Charging Rate	Nature
1	144-ton, liquid metal		first, 1 min of blow (stream 7)
2	11-ton, scrap	1.375 ton/min	first 8 min of blow at a constant rate (stream 8)
3	10.1-ton, lime	1.01 ton/min	first 2–11 min of blow at a fixed rate (stream 10)
4	3.2-ton, dolomite	0.35 ton/min	last 9 min of blowing at a constant rate (stream 11)
5	9000 Nm ³ , oxygen	455 Nm ³ /min	20 min at a constant rate (stream 13)

Sequence adjusted as per actual plant observations.

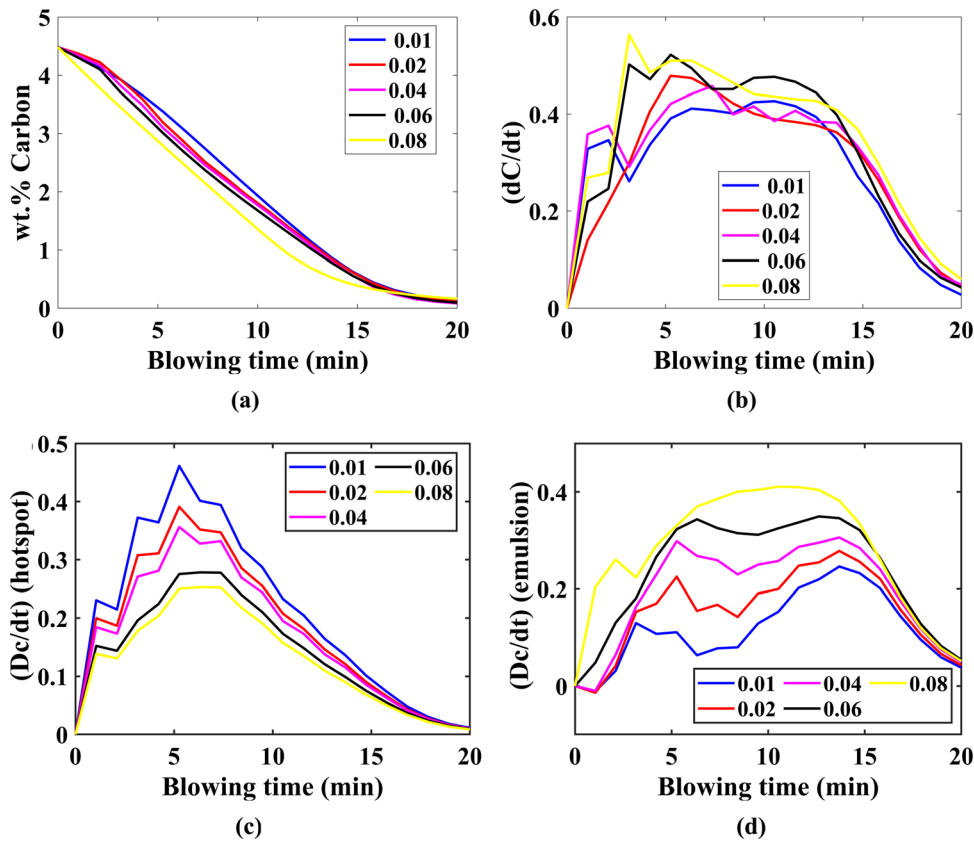


Fig. 2—Variations of wt pct carbon (a), total decarburization rate (b), decarburization from hotspot zone (c), and decarburization from emulsion zone (d) for different k values as a function of blowing time.

minute. Subsequently, for the duration of 6–15 minutes (6–15 min), these rates are measured at 0.288, 0.301, 0.315, 0.326, and 0.341 tons per minute. Towards the end of the blowing process (16–20 min), the decarburization rates are observed to be 0.092, 0.105, 0.118, 0.129, and 0.137 tons per minute, corresponding to the same k values. In terms of wt pct carbon, the terminal values achieved at the end of the blowing process for k values of 0.01, 0.02, 0.04, 0.06, and 0.08 are 0.086, 0.094, 0.116, 0.121, and 0.132, as depicted in Figure 2(a). Notably, the decarburization rate pattern exhibits an increase within the emulsion zone and a decrease within

the hotspot zone as k values escalate from 0.01 to 0.08, as exemplified in Figures 2(c) and (d), however total decarburization rate increased.

B. Transient Silicon Behaviors

Figure 3 depicts the graphical representation of variations in several parameters: wt pct silicon (‘a’), total desiliconization rate (‘b’), desiliconization from the hotspot zone (‘c’), and desiliconization from the emulsion zone (‘d’). These variations are examined across diverse emulsion zone size values as a function of the blowing time. During the initial 6 minutes (1–6 min), the

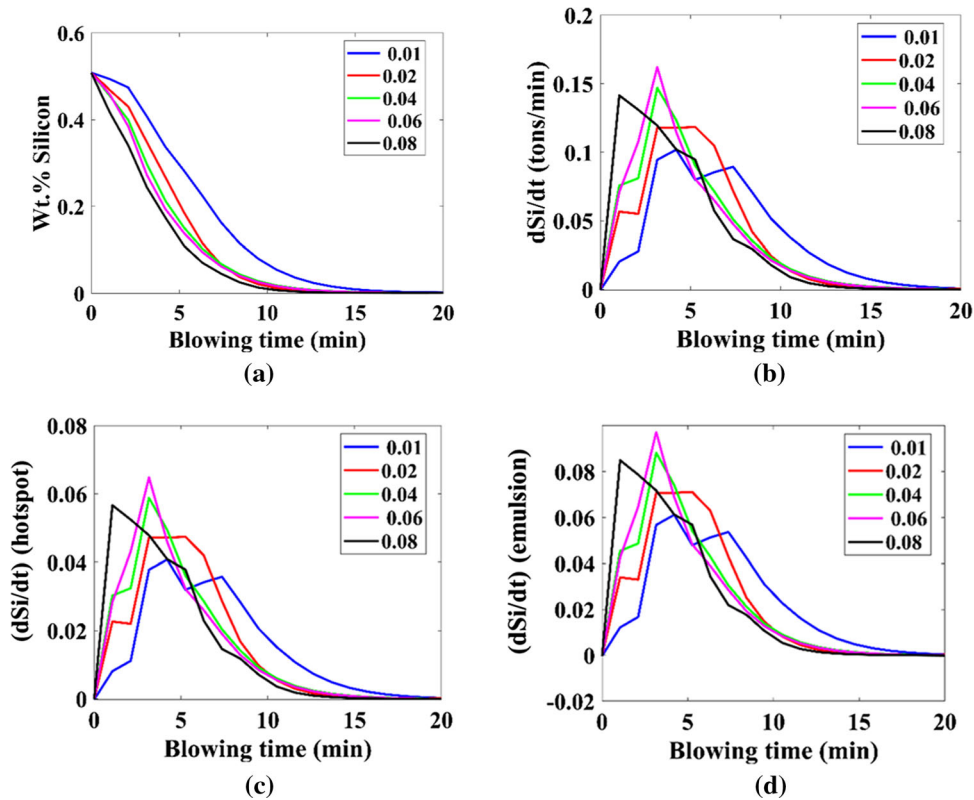


Fig. 3—Variations of wt pct silicon (a), total desiliconization rate (b), desiliconization from hotspot zone (c), and desiliconization from emulsion zone (d) for different k values as a function of blowing time.

desiliconization rates were 0.045, 0.064, 0.071, 0.073, and 0.079 tons per minute, corresponding to k values spanning from 0.01 to 0.08. However, during the subsequent time interval (11–20 min), the desiliconization rates became negligible. These observations are portrayed in Figure 3(b). Furthermore, the desiliconization rates displayed an upward trend in relation to increasing k values. Notably, the contribution of desiliconization from both the emulsion and hotspot zones remained equal, as highlighted in Figures 3(c) and (d), respectively.

C. Transient Phosphorus Behaviors

Figure 4 presents the graphical representation of variations in different parameters: wt pct phosphorus (‘a’), total dephosphorization rates (‘b’), dephosphorization from the hotspot zone (‘c’), and dephosphorization from the emulsion zone (‘d’). These variations are observed across various emulsion zone sizes as a function of the blowing time. It’s noteworthy that the initial 2 minutes exhibit minimal dephosphorization across all scenarios. Subsequently, dephosphorization rates for the duration of 3–16 minutes are measured at 0.00045, 0.000837, 0.001468, 0.001922, and 0.002183 tons per minute for k values ranging from 0.01 to 0.08. This information is graphically depicted in Figure 4(b). For the period spanning 17–20 minutes, the

dephosphorization rates were recorded as 0.000112, 0.000276, 0.000497, 0.000614, and 0.000687 tons per minute, for the same range of k values.

In terms of wt pct phosphorus, the terminal values are established at 0.0522, 0.0453, 0.0342, 0.0259, and 0.0209 for k values of 0.01 to 0.08, as indicated in Figure 4(a). Importantly, the dephosphorization process primarily originates from the emulsion zone, with the contribution from the hotspot zone being insubstantial.

D. Transient Slag Composition

Figure 5 depicts the weight percentages of slag components, specifically FeO (‘a’), CaO (‘b’), MgO (‘c’), and SiO₂ (‘d’), across a range of k values spanning from 0.01 to 0.08 as a function of blowing time. Within the first 7 minutes of blowing, there is a discernible decrease in wt pct FeO. During blowing time (8–20 minutes), wt pct FeO increases. Notably, as the blowing nears its conclusion, *i.e.*, between 16 and 20 minutes, there is a renewed increase in wt pct FeO across all the considered k values (0.01 to 0.08), as portrayed in Figure 5(a). Conversely, wt pct CaO increases during the initial 5 minutes of the blowing process and remains constant (6–12 minutes) of blowing, as illustrated in Figure 5(b). Regarding wt pct MgO, an upward trend is observed during the initial 11 minutes of the blowing process. However, towards the later phase (10–20 minutes) of blowing, there is a decline in both CaO

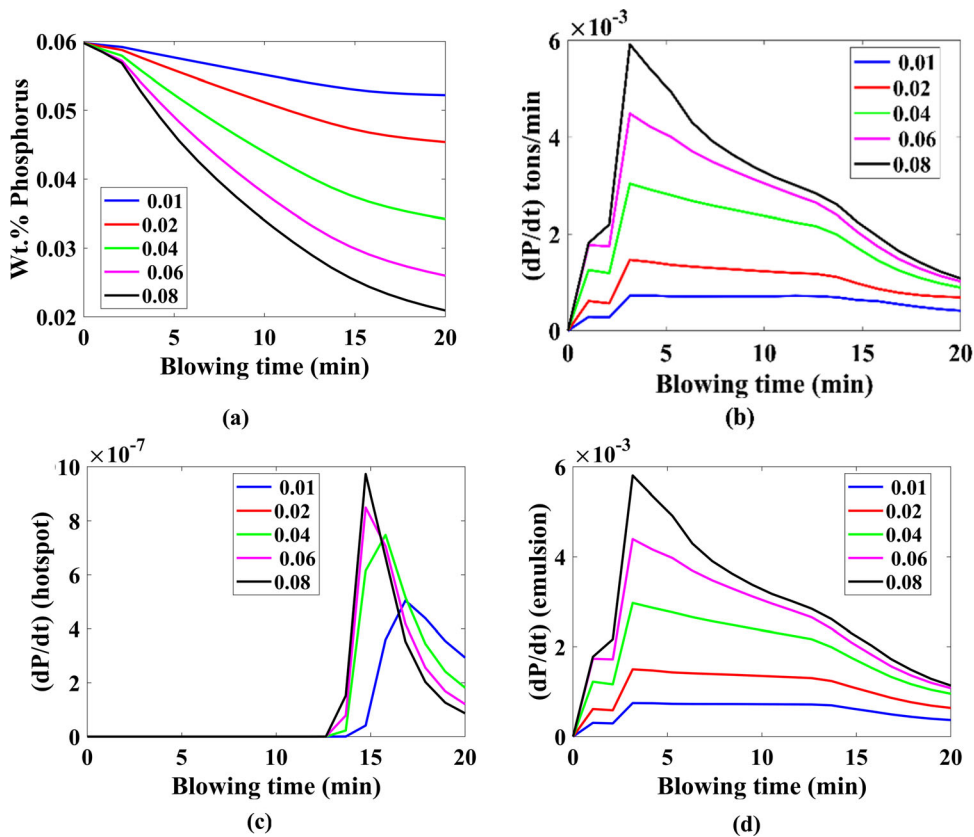


Fig. 4—Variations of wt pct phosphorus (a), total dephosphorization rate (b), dephosphorization from hotspot zone (c), and dephosphorization from emulsion zone (d) for different k values as a function of blowing time.

and MgO levels due to the dilution effect stemming from the presence of FeO. As for wt pct SiO₂, its increment is associated with higher k values. This phenomenon is linked to the elevated emulsion zone, resulting in a higher content of dissolved CaO and MgO due to presence of higher FeO content.

E. Transient Temperature

Figure 6 portrays the fluctuations in temperatures within the system: the metal bath temperature ('a'), the emulsion zone temperature ('b'), and the hotspot zone temperature ('c'). These variations correspond to distinct k values across the blowing time. The metal bath temperature exhibited a range spanning 1312 °C to 1738 °C, the emulsion zone temperature ranged from 1420 °C to 1800 °C, while the hotspot zone temperature displayed variability between 1750 °C and 2600 °C. Remarkably, alterations in the k values didn't lead to any observable changes in the temperature of both the metal bath and the emulsion zone. However, the hotspot zone temperatures demonstrated slight disparities across different k values. This discrepancy can be attributed to the distinct formations of FeO, exothermic reactions.

F. Validation with Plant Data

Figure 7 depicts variations in the percentages of carbon, silicon, and phosphorus, as well as the temperature of the metal bath, as a function of blowing time. The model predictions for carbon, silicon, and phosphorus, as well as the temperature of the metal bath, show good agreement with plant trials data when the k value is 0.06.

IV. DISCUSSION

The fractions of metal entering the hotspot and emulsion reactors, denoted as alpha (α) and beta (β), respectively, as well as the fraction of slag entering the emulsion reactor, referred to as gamma (γ), serve as indicators of mixing and mass transfer within the metal system. The oxygen entering the metal/gas reactor (reactor 3) is constant according to the volumetric flow rate. The fractions of bulk metal and bulk slag entering reactors 3 and 4 are the function of the system's top-blowing energy and bottom-stirring intensity. The details of the top and bottom stirring energy calculation are shown in Appendix 1. Several observations become

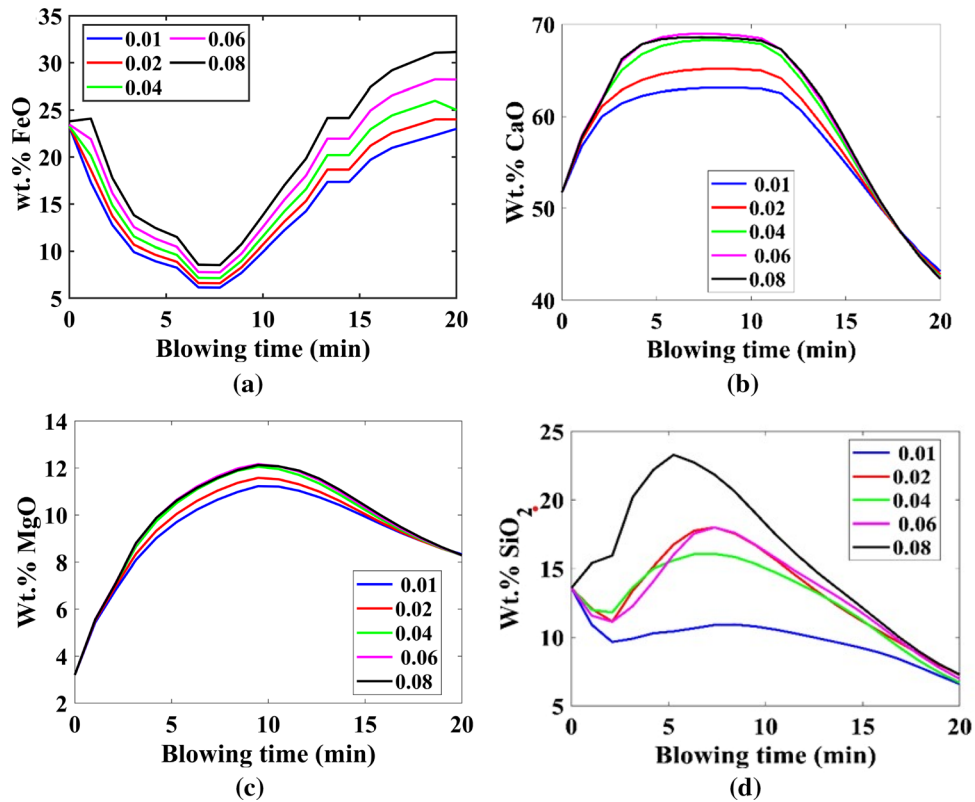


Fig. 5—Variation of wt pct FeO (a), wt pct CaO (b), wt pct MgO (c) and wt pct SiO₂ (d) for different k values as a function of blowing.

apparent when the metal flow rate is augmented to the emulsion reactor by varying the parameter k . A lower dephosphorization rate is noted at a lower k value (0.01), and the dephosphorization rate increases with increasing k value. The dephosphorization mechanism involves the oxidation of phosphorus, followed by its combination with $3\text{CaO}\cdot\text{P}_2\text{O}_5$ (C_3P) in the liquid slag, leading to the formation of a solid solution known as $2\text{CaO}\cdot\text{SiO}_2 - 3\text{CaO}\cdot\text{P}_2\text{O}_5$ ($\text{C}_2\text{S}-\text{C}_3\text{P}$). The dephosphorization phenomena during oxygen steelmaking are governed by mass transfer in the liquid slag phase and being dissolved in solid dicalcium or tricalcium silicate in slags, which have higher solubility for the phosphorus. The behavior of the emulsion zone influences the efficacy of phosphorus reduction because higher slag-metal interfacial area and oxidizing conditions are available favorably in the emulsion zone. Due to an increase in emulsion zone size, droplets of metal-gas and slag-metal, along with rising gases, experience an increase. Chemical reactions occur at the interfaces between gas-metal and slag-metal. Consequently, the interface area increases, leading to an enhanced decarburization rate in the emulsion zone. In the initial 1–5 minutes of blowing, a heightened lance position of 2.2 meters is upheld to ensure a slower decarburization rate, ranging between 0.178 to 0.221 tons per minute. As the process advances towards its end during the 16–20-minute interval, a reduced lance position of 1.62 meters is adopted. At this stage, carbon content falls below 0.35

pct. This shift results in elevated iron oxide (FeO) formation, decreasing the decarburization rate because the 16–20 minutes blowing period is marked by carbon levels dropping below the critical threshold of 0.35 pct, leading to the decarburization process primarily governed by mass transfer factors and oxygen reacting with iron to produce FeO. Consequently, the percentage of FeO increases during this (16–20 minutes) blowing phase.

At the lower k value (0.01), desilicization and dephosphorization rates remain lower due to inadequate formation of the emulsion zone. Nonetheless, the contribution to decarburization primarily stems from both the emulsion and hotspot zones. Consequently, the dephosphorization rate escalates as the volume of the emulsion zone increases (achieved by raising k values), while the SiO_2 content declines due to the facilitation of CaO dissolution by FeO, which then combines with SiO_2 . Decarburization is favored thermodynamically under conditions of high temperature and elevated FeO content. This explains the predominance of decarburization in the hotspot zone during the (1–9 min) due to the elevated temperature and a shift towards the emulsion zone towards the end of blowing (10–20 min) owing to the increased FeO content in the slag. While the model cannot forecast the reversion of phosphorus during the 5–10-minute blowing period, its predictive trajectory model proves valuable as a dependable guiding tool for optimizing real-world industrial

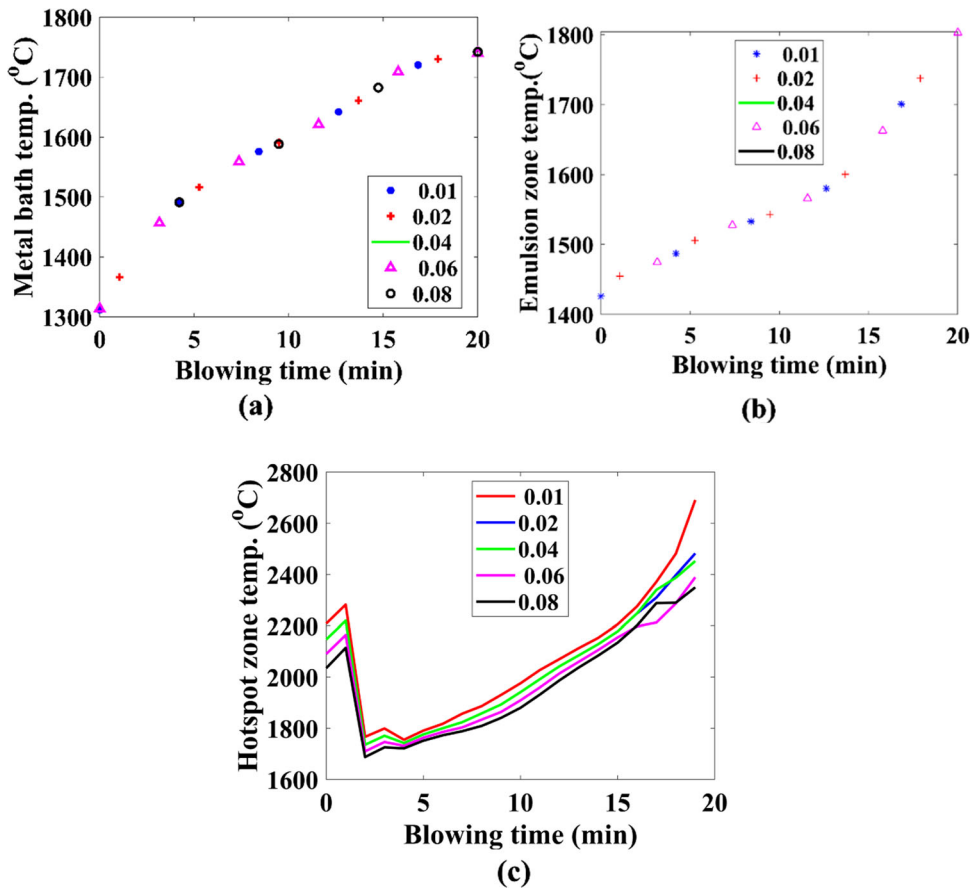


Fig. 6—The variation of metal bath temperature (a) and emulsion zone temperature (b), hotspot zone temperature (c) for different k values as a function of blowing time.

operations. Additionally, the model enables the separate assessment of carbon, silicon, and phosphorus removals in both the hotspot and emulsion zones of the basic oxygen furnace (BOF) steelmaking process, enhancing overall operational efficiency. In terms of dephosphorization, favorable conditions encompass low temperatures and the presence of adequate gas-metal and slag-metal interfaces

V. CONCLUSIONS

A mechanistic depiction of the refining phenomena's impact in the emulsion zones is presented. We draw the following conclusions from this investigation.

1. The decarburization, desiliconization, and dephosphorization predictions, along with the metal bath temperature, were found to be consistent with the plant trial data when considering a k value is 0.06.
2. Decarburization rates for k values of 0.01, 0.02, 0.04, 0.06, and 0.08 were found to be 0.178, 0.182, 0.191, 0.201, and 0.221 tons per minute during the initial 5 minutes (1–5 min), 0.288, 0.301, 0.315, 0.326 and 0.341 tons per minute during the subsequent 6–15 minutes, and 0.086, 0.094, 0.116, 0.121, and 0.132 tons per minute during the last 5 minutes of blowing (16–20 min).
3. The metal bath temperature exhibited a range spanning 1312 °C to 1738 °C, the emulsion zone temperature ranged from 1420 °C to 1800 °C, while the hotspot zone temperature displayed variability between 1750 °C and 2600 °C. Due to exothermic reactions, the hotspot zone temperature is elevated, primarily caused by the oxidation of carbon and iron.
4. The dephosphorization rate escalates as the volume of the emulsion zone increases (achieved by raising k values), while the SiO_2 content declines due to the facilitation of CaO dissolution by FeO , which then combines with SiO_2 . Decarburization is favored thermodynamically under conditions of high temperature and elevated FeO content.
5. In the context of refining reactions, the hotspot zone's involvement in dephosphorization seems negligible, with the emulsion zone emerging as the substantial contributor. However, when considering desiliconization and decarburization, the hotspot and emulsion zones display noteworthy participation as refining agents.

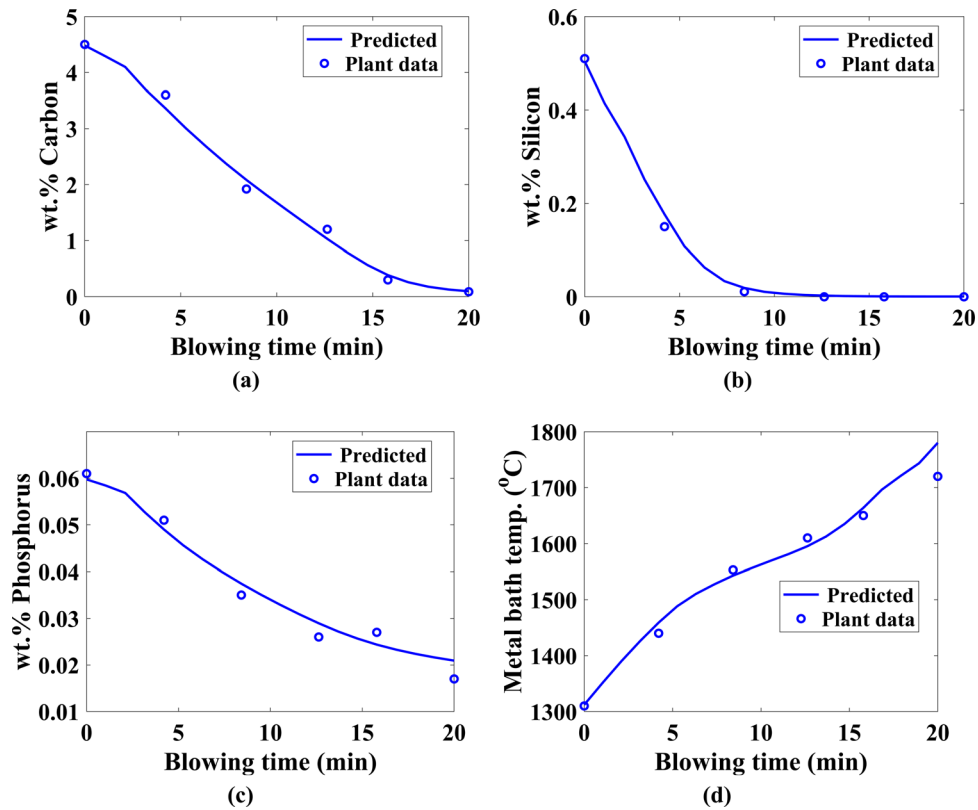


Fig. 7—Variation of predicted wt. pct carbon (a), silicon (b), phosphorus (c) and metal bath temperature (d) with plant data as a function of blowing time for k value 0.06.

ACKNOWLEDGMENTS

The author wishes to thank JSW Steel Ltd., India, for providing the plant data used to validate the models developed in this work.

FUNDING

No funding is available for this work.

CONFLICT OF INTEREST

The corresponding author states that there is no conflict of interest.

REFERENCES

1. Y. Ogasawara, Y. Miki, Y. Uchida, and N. Kikuchi: *ISIJ Int.*, 2013, vol. 53, pp. 1786–93.
2. F. Pahlevani, S.Y. Kitamura, H. Shibata, and N. Maruoka: *ISIJ Int.*, 2010, vol. 50, pp. 822–29.
3. X.R. Wu, P. Wang, L.S. Li, Z.J. Wu, and R.H. Chen: *Ironmak. Steelmak.*, 2011, vol. 38, pp. 185–88.
4. S. Barui, S. Mukherjee, A. Srivastava, and K. Chattopadhyay: *Metals*, 2019, vol. 9, pp. 1–8.
5. M. Iwasaki and M. Matsuo: *Nippon Steel Tech. Rep.*, 2011, vol. 391, pp. 88–93.
6. M. Kumakura: *Nippon Steel Tech. Rep.*, 2012, vol. 394, pp. 4–11.
7. M. Iwasaki and M. Matsuo: *Nippon Steel Tech. Rep.*, 2012, vol. 394, pp. 26–32.
8. T. Hashimoto, H. Iiboshi, and K. Kumar: *Nippon Steel Tech. Rep.*, 2012, vol. 394, pp. 84–90.
9. M. Kobayashi, K. Isobe, and M. Arai: *Nippon Steel Tech. Rep.*, 2012, vol. 394, pp. 119–24.
10. X.M. Yang, J.Y. Li, G.M. Chai, D.P. Duan, and J. Zhang: *Ironmak. Steelmak.*, 2017, vol. 44, p. 437.
11. X.M. Yang, C.B. Shi, M. Zhang, J.P. Duan, and J.A. Zhang: *Met. Mater. Trans. B.*, 2011, vol. 42, pp. 951–76.
12. F. He and L. Zhang: *J. Process. Control.*, 2018, vol. 66, pp. 51–58.
13. H. Sun, J. Yang, W. Yang, and R. Zhang: *Steel Res. int.*, 2023, vol. 94, pp. 1–21.
14. E. Turkdogan and J. Pearson: *ISIJ*, 1953, vol. 175, pp. 398–401.
15. E. Turkdogan and J. Pearson: *J. Iron Steel Inst.*, 1954, vol. 176, pp. 59–63.
16. G. Chen and S. He: *Ironmak. Steelmak.*, 2015, vol. 42, pp. 433–38.
17. T. Ikeda and T. Matsuo: *Trans. Iron Steel Inst. Jpn.*, 1982, vol. 22, pp. 495–503.
18. G. Ye, J. Yang, and Rh. Zhang: *Int. J. Miner. Metall. Mater.*, 2021, vol. 28, pp. 66–75.
19. X. Yang, F.M. Sun, J.L. Yang, F. Liu, F.K.S. Cheng, and J.H. Wang: *J. Iron. Steel Res. Int.*, 2013, vol. 20, p. 41.
20. B. Deo and R. Boom: *Fundamentals of Steel Making Metallurgy*, Prentice Hall International, Upper Saddle River, 1993.
21. K.S. Coley, E.Chen, and M. Pomeroy: in: *Proceedings of the Extraction and Processing Division Symposium on Pyrometallurgy*, San Diego, 16–20 June 2014, p. 289.
22. E. Chen and K.S. Coley: *Ironmak. Steelmak.*, 2010, vol. 37, pp. 541–45.
23. K. Gu, N. Dogan, and K.S. Coley: *Metall. Mater. Trans. B.*, 2017, vol. 48, pp. 2343–53.
24. K. Gu, N. Dogan, and K.S. Coley: *Metall. Mater. Trans. B.*, 2018, vol. 49, pp. 1119–35.
25. Z. Tian, B. Li, X. Zhang, and Z. Jiang: *J. Iron. Steel Res. Int.*, 2009, vol. 16, pp. 6–14.
26. W. Wu, S. Dai, and Y. Liu: *J. Iron. Steel Res. Int.*, 2017, vol. 24, pp. 908–15.
27. A. Basu, A.K. Lahiri, and S. Seetharaman: *Metall. Mater. Trans. B.*, 2007, vol. 38B, pp. 357–66.

28. A.N. Assis, M. Tayeb, S. Sridhar, and R.J. Fruehan: *Metals*, 2019, vol. 9, pp. 1–2.
29. Y. Zhou, R. Zhu, H. Wang, and H. Zhang: *Ironmak. Steelmak.*, 2021, vol. 48, pp. 570–78.
30. P. Kozakevitch: *Study of Basic Phosphate Slag Foams*, International Congress of Oxygen Steelmaking, Le Touquet, 1963.
31. H.W. Meyer, W.F. Porter, G.C. Smith, and J. Szekely: *JOM*, 1968, vol. 20, pp. 35–42.
32. S. Okano, J. Matsuno, H. Ooi, K. Tsuruoka, T. Koshikawa, and A. Okazaki: *International Conference on Science and Technology of Iron and Steel*, Iron and Steel Institute, Tokyo, 1971, pp. 227–31.
33. D.J. Price: *Process Engineering of Pyrometallurgy Symposium*, IMM, London, 1974.
34. A. Chatterjee, N.O. Lindfors, and J.A. Weste: *Ironmak. Steelmak.*, 1976, vol. 3, pp. 21–32.
35. B.K. Rout, G.A. Brooks, M.A. Rhamdhani, in: *Proceedings of the AISTech 2015 Iron and Steel Technology Conference*, Cleveland, 4–7 May 2015; vol. 3, pp. 3225–37.
36. B.K. Rout, G.A. Brooks, M.A. Rhamdhani, Z. Li, F.N.H. Schrama, and A. Overbosch: *Metall. Mater. Trans. B*, 2018, vol. 49, pp. 1022–1033.
37. N. Dogan, G.A. Brooks, and M.A. Rhamdhani: *ISIJ Int.*, 2011, vol. 51, pp. 1102–1109.
38. N. Dogan, G.A. Brooks, and M.A. Rhamdhani: *ISIJ Int.*, 2011, vol. 51, pp. 1093–1101.
39. P. Singha and A.K. Shukla: *Metals*, 2022, vol. 12, pp. 1–7.
40. D.G.C. Robertson, B. Deo, and S. Ohguchi: *Ironmak. Steelmak.*, 1984, vol. 11, pp. 41–56.
41. FactSage: Center for Research in Chemical Thermodynamics, Polytechnique de Montreal, Canada. Available online: www.factsage.com (accessed on 1 Feb 2023).
42. FactSage Documentation: version 7.3, 2021.
43. K.J. Graham and G.A. Irons: *Iron Steel Technol*, 2009, vol. 6, pp. 164–73.
44. P. Singha: *Ironmak. Steelmak.*, 2023, vol. 22, pp. 884–93.

Publisher's Note Springer Nature remains neutral with regard to jurisdictional claims in published maps and institutional affiliations.

Springer Nature or its licensor (e.g. a society or other partner) holds exclusive rights to this article under a publishing agreement with the author(s) or other rightsholder(s); author self-archiving of the accepted manuscript version of this article is solely governed by the terms of such publishing agreement and applicable law.